Published in final edited form as:
Nature. 2017 March 22; 543(7646): 525–528. doi:10.1038/nature21434.

Simultaneous tracking of spin angle and amplitude beyond classical limits

Giorgio Colangelo[1,*], **Ferran Martin Ciurana**[1], **Lorena C. Bianchet**[1], **Robert J. Sewell**[1], and **Morgan W. Mitchell**[1,2,†]

[1]ICFO-Institut de Ciencies Fotoniques, The Barcelona Institute of Science and Technology, 08860 Castelldefels, Barcelona, Spain

[2]ICREA – Institució Catalana de Recerca i Estudis Avançats, 08015 Barcelona, Spain

Abstract

Measurement of spin precession is central to extreme sensing in physics,1,2 geophysics,3 chemistry,4 nanotechnology5 and neuroscience,6 and underlies powerful magnetic resonance spectroscopies.7 Because there is no spin-angle operator, any measurement of spin precession is necessarily indirect, e.g., inferred from spin projectors F_α at different times. Such projectors do not commute, and thus quantum measurement back-action (QMBA) necessarily enters the spin measurement record, introducing errors and limiting sensitivity. Here we show how to reduce this disturbance below $\delta F_\alpha \sim \sqrt{N}$, the classical limit for N spins, by directing the QMBA almost entirely into an unmeasured spin component. This generates a planar squeezed state8 which, because spins obey non-Heisenberg uncertainty relations,9,10 allows simultaneous precise knowledge of spin angle and amplitude. We use high-dynamic-range optical quantum non-demolition measurements11–13 applied to a precessing magnetic spin ensemble, to demonstrate spin tracking with steady-state angular sensitivity 2.9 dB beyond the standard quantum limit, simultaneous with amplitude sensitivity 7.0 dB beyond Poisson statistics.14 This method for the first time surpasses classical limits in non-commuting observables, and enables orders-of-magnitude sensitivity boosts for state-of-the-art sensing15–18 and spectroscopy.19,20

Spin-based magnetometers monitor precession of the collective spin **F** of a magnetically-sensitive atomic ensemble,1,3,21 while atomic clocks2 and other atomic sensors22 use pseudo-spin systems with equivalent quantum descriptions: all are described by the SU(2) Lie algebra. Many optical interferometers are also SU(2) systems.23 These SU(2) systems obey different uncertainty relations than do position/momentum or harmonic oscillator systems, with dramatic consequences for their quantum sensitivity limits. The classical

Correspondence and requests for materials should be addressed to G.C. (giorgio.colangelo@icfo.eu) or M.W.M. (morgan.mitchell@icfo.eu).

Author Contributions

G.C. and F.M. performed the experiment, G.C analysed the results with the help of R.J.S., M.W.M. conceived the experiment and developed the theoretical model. All the authors designed the experiment, discussed the results and contributed to the manuscript.

Competing Interests

The authors declare no competing financial interests.

Europe PMC Funders Author Manuscripts

quantity to be measured manifests as precession rate $d\psi/dt$ about a known axis, which we take to be x. This signal is not directly observable, because there is no quantum mechanical operator for spin angle ψ. Rather, it must be estimated, e.g. from $F_z = |F_\rho| \cos \psi$, where $|F_\rho|$ is the spin amplitude in the y–z plane, itself an observable to be measured. While some theoretical models assume F_ρ to be precisely known *a priori*, this assumption cannot be applied to most systems of interest – relaxation necessarily adds noise not knowable *a priori*.24 We thus require a multi-component measurement: of amplitude and angle, or equivalently F_y and F_z, in both cases requiring tracking of non-commuting observables.

Similarly, magnetic resonance techniques20 employ simultaneous amplitude and angle tracking to correlate spin relaxation rate, which indicates the physical environment,19 with precession frequency, which indicates the chemical shift or, in imaging, the spin location.7 In these applications, joint angle-amplitude dynamics contain the important signal.

For simple harmonic oscillator systems, it is well known that QMBA couples angle and amplitude, or equivalently the quadratures X and P, as required to preserve the Heisenberg uncertainty relation $\delta X \delta P \geq 1/2$ (we take $\hbar = 1$ throughout). This limits angle tracking to the standard quantum limit25 (SQL), with uncertainty $\delta\psi = N^{-1/2}$, where here N is the mean number of excitations. In contrast, uncertainty principles do not prevent tracking spin systems beyond the SQL. As the spin components F_y and F_z precess about the x axis, they are governed by the Robertson (not Heisenberg) uncertainty relation9

$$\delta F_y \delta F_z \geq \frac{1}{2} |\langle [F_y, F_z] \rangle| = \frac{1}{2} |\langle F_x \rangle| . \quad (1)$$

In normal sensor operation, $\langle F_x \rangle$ is set to zero, to allow large polarization in the F_y–F_z plane. Because it is a constant of the motion, $\langle F_x \rangle$ remains zero for all time, and Eq. (1) places no limit on how precisely F_y and F_z can be simultaneously known or tracked. Arithmetic uncertainty relations10 then set the relevant limit, $\mathrm{var}(F_y) + \mathrm{var}(F_z) \sim N^{2/3}$, far below $\mathrm{var}(F_z) \sim N$, the SQL. Because N is typically $\sim 10^6$ in cold atom systems and $\sim 10^{12}$ in atomic vapors, this $N^{1/3}$ advantage extends the quantum limits by orders of magnitude. Spin states with two sub-classical spin uncertainties have been studied theoretically as *planar squeezed states*.8

Our discussion thus far indicates only the absence of uncertainty-principle barriers to precision spin tracking. We now outline a proof, given in Methods, that continuous quantum non-demolition (QND) measurement achieves this goal. The state evolution is illustrated in Fig. 1 a) and summarized here: F_z is coupled to an optical "meter" variable S_z via the QND interaction $H_{\mathrm{eff}} = gF_zS_z$, where g is a coupling constant. The interaction with N_L photons imprints a signal proportional to F_z on the meter, which when measured reduces $\mathrm{var}(F_z)$ by an amount $\Delta_\mathrm{m} \sim g^2 N_\mathrm{L} \mathrm{var}^2(F_z)$. This same interaction rotates $\mathbf{F}$ about F_z by a random angle $\theta \equiv gS_z$, which increases $\mathrm{var}(F_y)$ by $\Delta_\mathrm{d} \sim g^2 N_\mathrm{L} \mathrm{var}(F_x)$, much smaller than Δ_m, given that $\mathrm{var}(F_z) \gg 1$. Combining these effects, there is a net reduction of $\mathrm{var}(F_z) + \mathrm{var}(F_y)$, the total variance in the plane of precession. Precessing and under continuous measurement, F_z and F_y alternate roles as the measured and disturbed variable, and each experiences a net

uncertainty reduction. When N_L reaches $1/(g^2N)$, the measurement benefit $\Delta_m \sim N$ is of order the initial variance, while the in-plane back-action $\Delta_d \sim 1$ is still negligible. Probing with this N_L also induces a negligible loss of coherence, so that the sensitivity to both angular and radial perturbations improves beyond classical limits. It is important to note that the QMBA is not eliminated in this method, rather it is directed almost entirely to the F_x variable, which is never measured and acts as a depository for quantum uncertainty. A similar approach has been proposed for harmonic oscillators using auxiliary negative-mass oscillators to create uncertainty depositories.[26,27]

Realizing this in-principle advantage requires control of measurement dynamics[28] and incoherent effects,[29] as well as low-noise non-destructive detection with high dynamic range.[30] We use an ensemble of $N = 1.9 \times 10^6$ cold ^{87}Rb atoms held in an optical dipole trap. The atoms are initially prepared in the F_y-polarized state by optical pumping and, due to an applied B-field in the x direction, precess coherently in the F_y–F_z plane with Larmor period $T_L \approx 38$ μs. The "meter" variable is the polarisation of ~ 1 μs, off-resonance optical pulses, which experience Faraday rotation by an angle $\varphi = gF_z$ on the Poincare sphere as they propagate through the atomic cloud. We probe the atoms with V-polarized optical pulses, interspersed with Hpolarized compensation pulses to dynamically decouple the spin alignment,[12,13] i.e., to produce the effective hamiltonian $H_{\text{eff}} = gF_zS_z$ without tensor light shifts. Earlier experiments have demonstrated sub-projection noise Faraday rotation measurements of either angular[13] or amplitude[14] variables. To measure both, we use high dynamic-range, shot-noise-limited optoelectronics[30] and nonlinear signal reconstruction to achieve sub-projection-noise readout sensitivity for rotation up to $\varphi \approx 100$ mrad. See Methods.

A representative sequence of measured Faraday rotation angles $\varphi(t_k)$ for QND measurements spread over 1 ms is shown in Fig. 1 b), and is well described by a free induction decay model that we use to estimate F_z and F_y at a time t_e

$$\varphi(t) = g\left[F_z(t_e)\cos\omega_L t_r - F_y(t_e)\sin\omega_L t_r\right] e^{-t_r/T_2} + \varphi_0 \quad (2)$$

where $t_r \equiv t - t_e$. The coupling constant g is found by an independent calibration, while the Larmor frequency ω_L, the coherence time T_2, and the offset φ_0 are found by fitting to the measured $\varphi(t_k)$ over the the range $t_e - \Delta t \le t_k \le t_e + \Delta t$, where $\Delta t = 270$ μs (see Methods).

With these parameters fixed, we then use Eq. (2) to obtain a *predictive* estimate $\mathbf{F}_1 = \left(F_y^{(1)}, F_z^{(1)}\right)$ at time t_e using the measurements $\{\varphi(t_k)\}_{t_e-\Delta t \le t_k < t_e}$ from an interval Δt immediately *before* t_e; and to obtain a *confirming* estimate $\mathbf{F}_2 = \left(F_y^{(2)}, F_z^{(2)}\right)$ using $\{\varphi(t_k)\}_{t_e < t_k \le t_e+\Delta t}$ from the interval Δt after t_e. Because the classical parameters g, ω_L, T_2 and φ_0, are fixed beforehand, these are two linear, least-squares estimates of the vector $\mathbf{F}$ obtained from disjoint data sets. Estimating $\mathbf{F}$ for several values of t_e gives a predictive trajectory and a confirming one. We gather statistics over 453 repetitions of the experiment. Empirically, we find $\Delta t = 270$ μs minimizes the total conditional variance $\mathrm{Tr}(\Gamma_{\mathbf{F}_2|\mathbf{F}_1})$ (see

Methods), reflecting a trade-off of photon shot noise versus scattering-induced decoherence and magnetic-field technical noise.

Fig. 2 a) shows the resulting mean predictive trajectory $\langle \mathbf{F}_1 \rangle$, which spirals slowly toward the origin due to residual magnetic field gradient, and the discrepancy between the trajectories, $\mathbf{F}_2 - \mathbf{F}_1$. The scatter of this discrepancy rapidly decreases with increasing t_e, as more probe pulses become available for estimating $\mathbf{F}_1$, and reaches a steady state after about 250 μs of probing, at which point the number of pulses used for estimation is limited by Δt. With the optimum $\Delta t = 270$ μs, $N_p = 90$ and the total number of photons used to estimate $\mathbf{F}$ is $N_L = N_p \, . \, n_L = 2.47 \times 10^8$.

To quantify the measurement uncertainty, we compute the vector conditional covariance $\Gamma_{\mathbf{F}_2|\mathbf{F}_1} = \Gamma_{\mathbf{F}_2} - \Gamma_{\mathbf{F}_2\mathbf{F}_1} \Gamma_{\mathbf{F}_1}^{-1} \Gamma_{\mathbf{F}_1\mathbf{F}_2}$ where $\Gamma_{\mathbf{v}}$ matrix for vector $\mathbf{v}$, and $\Gamma_{\mathbf{uv}}$ indicates the cross-covariance matrix for $\mathbf{u}$ and $\mathbf{v}$. Defining the polar coordinate system $(F_y, F_z) = \rho(-\sin \psi, \cos \psi)$, we identify the radial and azimuthal variances, $\mathrm{var}(F_\rho) \equiv \hat{\rho}^T \Gamma_{\mathbf{F}_2|\mathbf{F}_1} \hat{\rho}$ and $\mathrm{var}(F_\psi) \equiv \hat{\psi}^T \Gamma_{\mathbf{F}_2|\mathbf{F}_1} \hat{\psi}$, respectively, where $\hat{\rho} \equiv (-\sin \psi, \cos \psi)^T$ and $\hat{\psi} \equiv (-\cos \psi, -\sin \psi)^T$ are radial and azimuthal unit vectors.

As shown in Fig. 2 c), $\mathrm{var}(F_\psi)$ drops below the SQL of $\langle F_\rho \rangle / 2$ after ≈ 150 μs of probing, and remains below it to the limit of the experiment. No read out noise has been subtracted. Considering the steady-state region $t_e \geq 270$ μs, $\mathrm{var}(F_\psi)$ is on average 2.9 dB below the SQL, and $\mathrm{var}(F_\rho)$ is on average 7.0 dB below the Poissonian variance N, to give a precision surpassing classical limits in both dynamical variables. For any given value of t_e, $\mathrm{var}(F_\rho)$ and $\mathrm{var}(F_\psi)$ have standard errors of ≈ 0.3 dB, implying high statistical significance even without combining results for different t_e.

We have shown how quantum measurement back-action can be almost completely evaded in spin-based sensors and spectroscopies, allowing simultaneous tracking of spin angle and amplitude beyond classical limits, using the physics of planar squeezed states.8 Our method is very close to practical application in the highest-performance atomic sensors: Tracking of atomic spin precession by non-destructive optical measurement is already used in the highest-sensitivity magnetic field measurements1 and is also being developed for optical lattice clocks.15 The method is compatible with multi-pass17 and cavity build-up methods, 18 that greatly reduce incoherent scattering, the limiting factor in our experiment. Together, these advances promise orders-of-magnitude sensitivity improvement in extreme sensing, in applications ranging from studies of macromolecular dynamics4 and geophysics,3 to non-invasive measurements of single-neurons6 and brain dynamics.16

Methods

A Faraday rotation probing of atomic spins

The effective atom-light interaction is given by the hamiltonian

$$H_{\mathrm{eff}} = g S_z F_z \quad (3)$$

Europe PMC Funders Author Manuscripts

which describes a quantum non-demolition measurement of the collective atomic spin F_Z, where the operators $F_\alpha \equiv \sum_i f_\alpha^{(i)}$ (with $\alpha = x, y, z$) describe the collective atomic spin, with $f_\alpha^{(i)}$ the spin orientation of individual atom spins. The optical polarization of the probe pulses is described by the Stokes operators $S_k = \frac{1}{2}\left(a_L^\dagger, a_R^\dagger\right)\sigma_k (a_L, a_R)^T$, with Pauli matrices σ_k. The coupling constant g depends on the detuning from the resonance, the atomic structure and the geometry of the atomic ensemble and probe beam and is independently measured.31–34,50

An input S_x-polarized optical pulse interacting with the atoms experiences a rotation by an angle $\varphi = gF_Z$ because of the interaction given by eq. (3). The transformation produced by the measurement on S_y is

$$S_y' = S_y \cos\varphi + S_x \sin\varphi \quad (4)$$

In our experiment we measure S_x at the input by picking off a fraction of the optical pulse and sending it to a reference detector, and S_y' using a fast home-built balanced polarimeter.35 Both signals are recorded on a digital oscilloscope.

From the record of S_x and S_y', we calculate $\hat{\varphi}$, the estimator for φ:

$$\begin{aligned}\hat{\varphi} &= \arcsin\left(\frac{S_y'}{S_x}\right)\\ &= \arcsin\left(\sin\varphi + \frac{S_y}{S_x}\sqrt{1-\sin^2\varphi}\right)\\ &= \varphi + \frac{S_y}{S_x} + \frac{1}{2}\left(\frac{S_y}{S_x}\right)^2 \tan\varphi + O\left(\frac{S_y}{S_x}\right)^3.\end{aligned} \quad (5)$$

We note that due to shot noise S_y/S_x is normally distributed with zero mean and variance $1/(2S_x) \sim 5\times10^{-7}$. The term containing $\tan\varphi$ thus describes a distortion of the signal at the $\sim 10^{-6}$ level, which is negligible in the experiment.

B Quantum limits for spin variances

Different classical limits provide benchmarks for the radial and azimuthal components of a spin precessing in the F_Y–F_Z plane. In general, these benchmarks describe the minimal noise of quantum states describing uncorrelated particles. For our system of N spin-1 atoms, the lowest noise uncorrelated state is the *coherent spin state* defined as a pure product state in which each atom is fully polarized in the same direction. If this direction is $\hat{y}\cos\theta - \hat{z}\sin\theta$, then the azimuthal component $F_\theta = -F_y \sin\theta + F_z \cos\theta$ has variance

$$\mathrm{var}\,(F_\psi)_{\mathrm{SQL}} = \frac{\langle F_\rho\rangle}{2}. \quad (6)$$

Any state that surpasses this limit implies entanglement among the atoms, and/or entanglement of the internal components of the individual atoms.36,37

For the radial component $F_\rho = F_y \cos\theta + F_z \sin\theta$, the classical limit comes from the fact that accumulation of independent atoms into the ensemble is limited by Poisson statistics, var(N) = $\langle N \rangle$, so that for $F = 1$,

$$\mathrm{var}\,(F_\rho)_{\mathrm{Poisson}} = \langle N \rangle . \quad (7)$$

Noise below this level can be produced by a strong interaction among the atoms during accumulation,38–41 or as here by precise non-destructive measurement.34,42–47

C Operator-level description of back-action evading measurement of two non-commuting spin observables

We consider a spin variable **F**, defined by commutation relations $[F_x, F_y] = iF_z$ and cyclic permutations, precessing about the F_x axis and subjected to brief, non-destructive measurements of the F_z variable. We assume the precession during the measurement is negligible. In the measurement, the spin is coupled to the polarization of a probe pulse, described by the Stokes operators **S** with $[S_x, S_y] = iS_z$ and cyclic permutations. The probe initial state is a coherent state polarized along S_x, so that

$|\langle S_x \rangle| = N_{\mathrm{L}}/2, \langle S_y \rangle = \langle S_z \rangle = 0,$ and $\mathrm{var}\,(S_y) = \mathrm{var}\,(S_z) = \frac{1}{2}|\langle S_x \rangle|$. The system and meter are coupled by the quantum nondemolition hamiltonian

$$H_{\mathrm{eff}} = gS_zF_z \quad (8)$$

which acts for unit time. The transformation produced is

$$S_x' = S_x \cos gF_z - S_y \sin gF_z \quad (9)$$

$$S_y' = S_y \cos gF_z + S_x \sin gF_z \quad (10)$$

$$S_z' = S_z \quad (11)$$

$$F_x' = F_x \cos gS_z - F_y \sin gS_z \quad (12)$$

$$F_y^{'}=F_y\cos gS_z+F_x\sin gS_z \quad (13)$$

$$F_z^{'}=F_z \quad (14)$$

Where primes indicate the output variables.

We assume a spin state in the F_y-F_Z plane, i.e. with $\langle F_X\rangle = 0$, and with zero initial cross-correlation, i.e. $\mathrm{cov}(F_X , F_y) = \mathrm{cov}(F_X , F_Z) = 0$. Due to the zero mean of S_Z, which is also independent of **F**, the transformation preserves these statistics in the primed variables, for example

$$\mathrm{cov}\left(F_x^{'},F_y^{'}\right)=\mathrm{cov}\left(F_x,F_y\right)\left\langle\cos^2 gS_z-\sin^2 gS_z\right\rangle+\left[\mathrm{var}\left(F_x\right)+\mathrm{var}\left(F_y\right)\right]\langle\cos gS_z\sin gS_z\rangle=0 \quad (15)$$

We can compute the statistics of the output variables using

$$\begin{aligned}\langle\cos gS_z\rangle&=\left\langle 1-\tfrac{1}{2}g^2\mathrm{var}\left(S_z\right)+O(g)^4\right\rangle\\&=1-\tfrac{1}{4}g^2\left|\langle S_x\rangle\right|+O(g)^4\end{aligned} \quad (16)$$

and similar expansions for $\langle\cos^2 gS_Z\rangle$ and $\langle\sin^2 gS_Z\rangle$. The mean of F_y changes due to the back-action as

$$\begin{aligned}\left\langle F_y^{'}\right\rangle&=\langle F_y\rangle\langle\cos gS_z\rangle+\langle F_x\rangle\langle\sin gS_z\rangle\\&=\langle F_y\rangle\langle\cos gS_z\rangle\\&=\langle F_y\rangle-\tfrac{1}{4}g^2\left|\langle S_x\rangle\right|\langle F_y\rangle+O(g)^4\end{aligned} \quad (17)$$

while the means of F_X and F_Z are unchanged.

The variance of F_X is coupled to the variance of F_y, due to the rotation about F_Z by a random angle gS_Z:

$$\begin{aligned}\mathrm{var}\left(F_x^{'}\right)&=\left\langle\left(F_x\cos gS_z-F_y\sin gS_z\right)^2\right\rangle-\langle F_y\rangle^2\langle\mathrm{sin}gS_z\rangle^2\\&=\mathrm{var}\left(F_x\right)\langle\cos^2 gS_z\rangle+\left\langle F_y^2\right\rangle\langle\sin^2 gS_z\rangle\\&=\mathrm{var}\left(F_x\right)+g^2\left|\langle S_x\rangle\right|\left[-\tfrac{1}{4}\mathrm{var}\left(F_x\right)+\tfrac{1}{2}\left\langle F_y^2\right\rangle\right]+O(g)^4\end{aligned} \quad (18)$$

and similarly

$$\begin{aligned}\mathrm{var}\left(F_y^{'}\right) &= \left\langle \left(F_y \cos gS_z + F_x \sin gS_z\right)^2 \right\rangle - \langle F_y\rangle^2 \langle \cos gS_z\rangle^2 \\ &= \left\langle F_y^2 \cos^2 gS_z \right\rangle + \langle F_x^2 \sin^2 gS_z\rangle - \langle F_y\rangle^2 \langle \cos gS_z\rangle^2 \\ &= \left\langle F_y^2 \right\rangle \langle \cos^2 gS_z\rangle - \langle F_y\rangle^2 \langle \cos gS_z\rangle^2 + \langle F_x^2\rangle \langle \sin^2 gS_z\rangle \\ &= \mathrm{var}\left(F_y\right) + g^2 \left|\langle S_x\rangle\right| \left[-\tfrac{1}{4}\mathrm{var}\left(F_y\right) + \tfrac{1}{2}\mathrm{var}\left(F_x\right)\right] + O(g)^4 \end{aligned} \quad (19)$$

after noting that, to order g^3, $\langle \cos^2 gS_z\rangle = \langle \cos gS_z\rangle^2$.

After the coupling, a projective measurement of $S_y^{'}$ provides information about F_z, with readout variance

$$\mathrm{var}_{\mathrm{RO}}\left(F_z\right) \approx \frac{1}{2g^2 \left|\langle S_x\rangle\right|}. \quad (20)$$

The approximation comes from a linearization of Eq. (10), which as discussed in Sec. A introduces an error at the 10^{-6} level, negligible in this scenario.

The resulting F_z variance, including both the prior and posterior information, is then[48,49]

$$\begin{aligned}\mathrm{var}\left(F_z^{'}\right) &= \frac{1}{\mathrm{var}^{-1}\left(F_z\right) + \mathrm{var}_{\mathrm{RO}}^{-1}\left(F_z\right)} \\ &= \frac{\mathrm{var}\left(F_z\right)}{1 + 2g^2 \left|\langle S_x\rangle\right| \mathrm{var}\left(F_z\right)} \end{aligned} \quad (21)$$

expanding in g this becomes

$$\mathrm{var}\left(F_z^{'}\right) = \mathrm{var}\left(F_z\right) - 2g^2 \left|\langle S_x\rangle\right| \mathrm{var}^2\left(F_z\right) + O(g)^4. \quad (22)$$

Collecting Eqs. (18), (19) and (22), defining

$\Delta\langle F_\alpha\rangle \equiv \left\langle F_\alpha^{'}\right\rangle - \langle F_\alpha\rangle$ and $\Delta\mathrm{var}\left(F_\alpha\right) \equiv \mathrm{var}\left(F_\alpha^{'}\right) - \mathrm{var}\left(F_\alpha\right)$, and dropping terms of order $O(g)^4$ we find

$$\Delta\langle F_y\rangle = -\frac{1}{2} g^2 \left|\langle S_x\rangle\right| \langle F_y\rangle \quad (23)$$

$$\Delta\mathrm{var}\left(F_x\right) = g^2 \left|\langle S_x\rangle\right| \left[-\frac{1}{4}\mathrm{var}\left(F_x\right) + \frac{1}{2}\left\langle F_y^2\right\rangle\right] \quad (24)$$

Europe PMC Funders Author Manuscripts

$$\Delta \mathrm{var}\,(F_y) = g^2\,|\langle S_x\rangle|\left[-\frac{1}{4}\mathrm{var}\,(F_y)+\frac{1}{2}\mathrm{var}\,(F_x)\right] \quad (25)$$

$$\Delta \mathrm{var}\,(F_z) = -\,2g^2\,|\langle S_x\rangle|\,\mathrm{var}^2\,(F_z) \quad (26)$$

Considering an initial coherent spin state and choosing $|\langle S_x\rangle| = g^{-2}N^{-1}$, where N is the number of spins, we note that $\Delta\mathrm{var}(F_z) \sim N$, implying a reduction in the uncertainty of F_z comparable to its initial uncertainty. Due to the $\left\langle F_y^2\right\rangle$ term, the increase in $\mathrm{var}(F_x)$ is $\sim N$, comparable to its initial value. The other changes are ~ 1, negligible relative to the initial values. In this way we see that uncertainty is moved from F_z to F_x with negligible effect on F_y.

Larmor precession then noiselessly rotates uncertainty from F_y into F_z, uncertainty that is moved into F_x by the next measurement. This procedure reduces the uncertainty of both F_y and F_z with negligible in uence from measurement back-action.

D Implementation in an atomic ensemble

1 Experimental set up—The experimental set up is described in detail in references . 31,50 The trap consists of a single beam laser at 1064 nm with 6.3 W of optical power, focused to a beam waist of 26 μm using an 80 mm lens. The trap is loaded with laser-cooled atoms from a magneto optical trap (MOT). After sub-doppler cooling in the final stage of the loading sequence, the trapped atoms have a temperature ~ 12 μK. The resulting atomic ensemble has an approximately Lorentzian distribution along the trap axis (which we label the z-axis) with a FWHM of $w = 4$ mm, and a gaussian distribution in the radial direction with of $\omega = 33 \pm 3$μm.

2 State preparation—The initial atomic state is prepared via optical pumping with circularly polarized light resonant with the $F = 1 \rightarrow F' = 1$ transition propagating along the y-axis. During the optical pumping stage the atoms are also illuminated with repumping light resonant with the $F = 2 \rightarrow F = 2'$ transition using the six MOT beams, preventing accumulation of atoms in the $F = 2$ hyperfine level, and a small magnetic field is applied along the x-axis, with $B_x = 37.6$ mG, to coherently rotate the atomic spins in the y–z plane. We use a stroboscopic pumping strategy, chopping the optical pumping light into a series of $\tau_{\mathrm{pump}} = 1.5$ μs duration pulses applied synchronously with the precessing atoms for total of 200 μs, to prepare the atoms in an F_y-polarized state with high efficiency (~ 98%), resulting in a input polarized atomic ensemble with $\langle F_y\rangle \simeq N$ (see Extended Data Fig. 1). The pulse duration $\tau_{\mathrm{pump}} \ll T_L$ is chosen to optimize the optical pumping efficiency.

3 Probing—We probe the atoms via off-resonant paramagnetic Faraday-rotation using $\tau = 0.6$ μs duration pulses of linearly polarized light with a detuning of 700 MHz to the red of the ^{87}Rb D_2 line. The probe pulses are V-polarized, with on average $N_{\mathrm{L}} = 2.74 \times 10^6$

photons, and sent through the atomic cloud at 3 μs intervals. Between the probe pulses, we send *H*-polarized compensation pulses with on average $N_{\mathrm{L}}^{(\mathrm{H})}=1.49\times10^{6}$ photons through the atomic cloud. As described in detail in references,48,51,52 the compensation pulses serve to cancel effects due to the tensor light shift, but do not otherwise contribute to the measurement. During the probing sequence, a magnetic field along the *x* direction drives a coherent rotation of the atoms in the $y-z$ plane with $T_L = 38$ μs period. This ensures that the time taken to complete a single-pulse measurement is small compared to the Larmor precession period, i.e. $\tau \ll T_L$.

We correct for slow drifts in the polarimeter signal by subtracting a baseline $\varphi_0=\frac{1}{N}\sum_{k=1}^{N}\varphi_k^{(i)}$ from each pulse, estimated by repeating the measurement without atoms in the trap.

4 Statistics of probing inhomogeneously-coupled atoms—We consider the statistics of Faraday rotation measurements on an ensemble of N atoms, described by individual spin operators $\mathbf{f}_i$. To define the SQL, we consider an ensemble in a coherent spin state, with the individual spins are independent and fully polarized in the F_y–F_z plane. We take N to be Poisson-distributed. When the spatial structure of the probe beam is taken into account, the Faraday rotation is described by the input-output relation for the Stokes component S_y

$$S_y^{(\mathrm{out})}=S_y^{(\mathrm{in})}+S_x^{(\mathrm{in})}\sum_{i=1}^{N}g(\mathbf{x}_i)f_z^{(i)} \tag{27}$$

where $g(\mathbf{x}_i)$ is the coupling strength for the ith atom, proportional to the intensity at the location $\mathbf{x}_i$ of the atom. $S_y^{(\mathrm{in})}$ is has zero mean and variance $|\langle S_x^{(\mathrm{in})}\rangle|/2$. We consider first the case in which the spin is orthogonal to the measured F_z direction, i.e. a measurement of the azimuthal component. Here the uncertainty in $g(\mathbf{x}_i)$ and in N make a negligible contribution, and the rotation angle $\varphi=S_y^{(\mathrm{out})}/S_x^{(\mathrm{in})}$ has the statistics

$$\langle\varphi\rangle=\langle f_z\rangle\sum_{i=1}^{N}\langle g(\mathbf{x}_i)\rangle_{\mathbf{x}_i}\equiv\langle N\rangle\langle f_z\rangle\mu_1 \tag{28}$$

$$\mathrm{var}\,(\varphi)=\mathrm{var}\,(\varphi_0)+\mathrm{var}\,(f_z)\left\langle\sum_{i=1}^{N}g^2(\mathbf{x}_i)\right\rangle_{N,\mathbf{x}_i}\equiv\mathrm{var}\,(\varphi_0)+\langle N\rangle\,\mathrm{var}\,(f_z)\,\mu_2 \tag{29}$$

where φ_0 is the polarization angle of the input light, subject to shot-noise fluctuations and assumed independent of F_z, and the angle brackets indicate an average over the number and positions of the atoms.

Next we consider the case in which the spin is along the measured F_z direction, i.e., a measurement of the radial component. In this case, the uncertainty in f_z is zero, and the variation in g and in N determines the measured variation

$$\langle\varphi\rangle = \langle N\rangle \langle f_z\rangle \mu_1 \quad (30)$$

$$\mathrm{var}(\varphi) = \mathrm{var}(\varphi_0) + \langle f_z\rangle^2 \mathrm{var}\left(\sum_{i=1}^{N} g(\mathbf{x}_i)\right) \equiv \mathrm{var}(\varphi_0) + \langle N\rangle \langle f_z\rangle^2 v_2 \quad (31)$$

We note that v_2 includes the variation of both the atom number and the coupling strength, and as such is lower-bounded by the Poisson statistics of N: $v_2 \geq \langle g^2(\mathbf{x})\rangle = \mu_2$.

For known $\langle f_z\rangle$ and var(f_z), measurements of $\langle\varphi\rangle$ and var(φ) versus N give the calibration factors μ_1 and μ_2 as described in Sections D5 and D6, respectively. To preserve the SQL $\mathrm{var}(F_z) = \frac{1}{2}|\langle F_y\rangle|$ and similar, in the analysis leading to Fig. 2 we infer mean values as

$$\left\langle F^{(a)}\right\rangle = \frac{1}{\mu_1}\left\langle \varphi^{(a)}\right\rangle \quad (32)$$

and covariances, including cov(A, A) = var(A), as

$$\mathrm{cov}\left(F^{(a)}, F^{(b)}\right) = \frac{1}{\mu_2}\mathrm{cov}\left(\varphi^{(a)}, \varphi^{(b)}\right), \quad (33)$$

where $F^{(a,b)}$ and $\varphi^{(a,b)}$ are corresponding spin and angle variables. We note that because the contribution of var(φ_0) is not subtracted, this overestimates the spin variances.

5 Measurement of calibration factor μ_1—We calibrate the measured rotation angle φ with a dispersive atom number measurements using absorption imaging, as shown in Extended Data Fig. 2. For the absorption imaging, atoms are transferred into the $f = 2$ hyperfine ground state by a 100 μs pulse of laser light tuned to the $5S_{1/2}(f = 1) \rightarrow 5P_{3/2}(f' = 2)$ transition. The dipole trap is switched off to avoid spatially dependent light shifts. An image is taken with a 100 μs pulse of circularly polarized light resonant to the $5S_{1/2}(f = 2) \rightarrow 5P_{3/2}(f' = 3)$ transition. We calculate the resonant interaction cross-section and take into account the finite observable optical depth. The statistical error in the absorption imaging is < 3%, including imaging noise and shot-to-shot trap loading variation.

6 Measurement of calibration factor μ_2—To measure μ_2 we prepare a F_y-polarized state by optical pumping, and then probe stroboscopically with $N_p = 36$ pulses of $N_L = 3.15 \times 10^7$ photons each in the presence of a B-field of ≈ 71.5 mG along y, producing a Larmor

precession of an angle π during the 10 μs pulse repetition period. In this way, the measured variable is always $\pm F_z$, evading back-action effects.

If φ_n is the measured Faraday rotation angle for pulse n, and $\varphi_0^{(n)}$ is the corresponding input angle, we can define the pulse-train-averaged rotation signal as

$$\varphi \equiv \frac{1}{N_\mathrm{p}} \sum_{n=1}^{N_\mathrm{p}} (-1)^{n-1} \varphi_n \tag{34}$$

with variance

$$\mathrm{var}(\varphi) \equiv \mathrm{var}(\varphi_0) + \mu_2 \sum_{n=1}^{N_\mathrm{p}} \mathrm{var}(F_{z,n}) \tag{35}$$

where $\varphi_0 = \frac{1}{N_\mathrm{p}} \sum_{n=1}^{N_\mathrm{p}} \varphi_o^{(n)}$; with zero mean and variance $\mathrm{var}(\varphi_0) = (N_\mathrm{p} N_\mathrm{L})^{-1}$, and $F_{z,n}$ is the value of F_z at the time of the nth probe pulse.

During the measurement, off-resonant scattering of probe photons produces both a reduction in the number of probed atoms and introduces noise into **F**. We note that this is a single-atom process that preserves the independence of the atomic spins. We compute the resulting evolution of the state using the covariance matrix methods reported in,48 and specifically described for this case in Section D7, giving

$$\mathrm{var}\left(\frac{g}{N_\mathrm{p}} \sum_{n=1}^{N_\mathrm{p}} F_{z,n} \right) = \mu_2 \frac{1}{2} \alpha N \tag{36}$$

where $1/2 = \mathrm{var}(f_z)$ is the variance of the initial state, $\alpha = 0.86$ describes the net noise reduction due to scattering.

Including the readout noise $\mathrm{var}(\varphi_0)$ and a generic technical noise $a_2 N^2$ in the preparation of the coherent spin state, we have the observable variance

$$\mathrm{var}(\varphi) = \mathrm{var}(\varphi_0) + \mu_2 \frac{1}{2} \alpha N + a_2 N^2, \tag{37}$$

in which the N scaling distinguishes the atomic quantum noise from other contributions. Experimental result shown in Extended Data Fig. 3 give $\mu_2 = (1.5 \pm 0.2) \times 10^{-14}$.

7 Calculation of the noise contribution α—As reported in Colangelo et al.48 the full system is described by a state vector $V = \left\{ F_z, S_y^{(1)}, S_y^{(2)}, \ldots, S_y^{(N)} \right\}$ and covariance

matrix $\Gamma = \langle V \wedge V + (V \wedge V)^T \rangle/2 - \langle V \rangle \wedge \langle V \rangle$, where S_y^n is the measured photon imbalance after the n-th pulse. The QND interaction leads to a transformation of the covariance matrix

$$\Gamma^{(n+1)} = \mathbf{M}^{(n)} \Gamma^{(n)} [\mathbf{M}^{(n)}]^T \quad (38)$$

where $\mathbf{M}$ is equal to the identity matrix apart from the elements $\mathbf{M}_{1,1} = -1$ due to the precession by an angle π about the magnetic field, and $\mathbf{M}_{n+1,1} = gS_x$, where $S_x = N_L/2$ and N_L is the number of photons per pulse and g is the coupling constant for uniform coupling.

Off-resonant scattering of photons introduces decoherence, noise and loss in the atomic state. During the spin-noise measurement, a fraction $\xi = 1 - \exp(-\eta N_L) = 0.01$ of atoms scatter a photon during a single probe pulse, where $\eta = 3 \times 10^{-10}$ is the scattering rate per photon measured in an independent experiment, while a fraction $\chi = 1 - \xi$ remain in the coherent spin state. The scattered atoms are either lost from the $F = 1$ manifold, or return to $F = 1$ with probability $p = 0.7$ and random polarization. This has the effect of losing atomic polarization at each measurement. We calculate the effective measured polarization in terms of the initial atom number. We assume that the fraction p of scattered atoms the return to $F = 1$ have a random polarization and that the scattering rate η is independent of the atomic state.

After each pulse, the atomic part of the covariance matrix transforms according to

$$\Gamma_{\mathrm{at}}^{(n+1)} = \chi \Gamma_{\mathrm{at}}^{(n)} + \frac{2}{3} p(1-\chi) N^{(n)} \mathbb{I} \quad (39)$$

where $\mathbb{I}$ is the identity matrix. This follows from Eq.(A.6) of48 assuming $\Gamma_\wedge = N\Gamma_\lambda$. We note that we have

$$N^{(n+1)} = 1 - (1-\chi)(1-p) N^{(n)} = (\chi + p - \chi p) N^{(n)} \quad (40)$$

which, assuming that $N^{(0)} = N$, gives

$$N^{(n)} = (\chi + p - \chi p)^n N \quad (41)$$

Including these terms, we get a linear transformation of the covariance matrix after the n-th pulse

$$\Gamma^{(n+1)} = \mathbf{D}\mathbf{M}^{(n)} \Gamma^{(n)} [\mathbf{M}^{(n)}]^T \mathbf{D}^T + \mathbf{N}^{(\mathbf{n})} \quad (42)$$

where $\mathbf{D}$ is a zero matrix apart from the element $\mathbf{D}_{1,1} = \sqrt{\chi}$, and $\mathbf{N}^{(\mathbf{n})}$ is the identity matrix apart from the element $\mathbf{N}^{(\mathbf{n})} 1,1 = \frac{2}{3} p(1-\chi)(\chi + p - \chi p)^n N$.

We sum N individual polarimeter signals $S_y^{'(n)}$ to find the net Stokes operator $S_y^{'} \equiv \sum_{n=1}^{N} (-1)^{n-1} S_y^{'(n)}$. This has a variance

$$\begin{aligned} \mathrm{var}(S_y^{'}) &= \sum_{n=1}^{N} \mathrm{var}(S_y^{'(n)}) + 2 \sum_{n \neq m}^{N} \mathrm{cov}(S_y^{'(n)}, S_y^{'(m)}) (-1)^{n-m} \\ &= \mathbf{P} \Gamma^{(N)} \mathbf{P} \end{aligned} \tag{43}$$

with the projector $\mathbf{P} = \mathrm{diag}(0, 1, -1, 1, -1, \ldots, -1)$. When evaluated analytically using $\chi = 0.99$, this gives

$$\mathrm{var}(S_y^{'}) = \mathrm{var}(S_y, 0) + \beta g^2 \frac{1}{2} N N_{\mathrm{L}}^2 \tag{44}$$

where $\beta \approx 0.1081$. Noting that $\mathrm{var}(\varphi) = \mathrm{var}(S_y^{'})/S_x^2$, where $S_x \equiv \sum_{n=1}^{N} S_x^{(n)}$ is the total input Stokes operator, dividing Eq. (44) by $S_x^2 = N_{\mathrm{L}}^2/4$, and comparing against Eq. (37), we find that $\alpha = 8\beta \approx 0.86$.

E Data analysis

1 Fitting procedure—As described in the main text, we follow a two-step fit procedure in our data analysis: we first fit Eq. 2 to the joint data set $\{\varphi(t_k)\}$ of the first and second measurements, to estimate the classical parameters g, ω_{L}, T_2 and φ_0 near the measurement time t_{e}; then second, with the classical parameters fixed, we obtain a *predictive* estimate $\mathbf{F}_1$ using measurements $\{\varphi(t_k)\}_{t_{\mathrm{e}}-\Delta t \leq t_k < t_{\mathrm{e}}}$ from the interval Δt immediately *before* t_{e}; and a *confirming* estimate $\mathbf{F}_2$ using $\{\varphi(t_k)\}_{t_{\mathrm{e}} < t_k \leq t_{\mathrm{e}}+\Delta t}$ from the interval Δt *after* t_{e}.

2 Measurement phase—We note that, as shown in Fig. 2, the observed squeezing is independent of the choice of t_{e} provided that sufficient measurements are available in the interval Δt prior to t_{e}, indicating that the observed squeezing is not dependent on the choice of a particular phase of the spin oscillation.

3 Fit gain—Since the classical parameters g, ω_{L}, T_2 and φ_0 are fixed beforehand, the predictive and confirming fits to estimate F_y and F_z are linear, least-squares fits to disjoint data sets. We note that our condition for (conditional) spin squeezing is whether the conditional variance $\mathrm{Tr}(\Gamma_{\mathbf{F}_2|\mathbf{F}_1})$ is below classical limits - i.e., whether the estimate $\mathbf{F}_1$ can be used to precisely predict the estimate $\mathbf{F}_2$. This definition of squeezing is quite robust as regards the choice of estimators for F_y and F_z: they only need to have the right *gain*, i.e., the slope of the curve relating the mean estimate to the true value. The error propagation formula can then be used to find the variance of the true values in terms of the variance of the estimators.

We check that the least-squares fits give the correct gain by comparing the estimated $\mathbf{F}_{1,2}$ with the results of two independent fits using all free parameters in Eq. (2). Results, shown

in Extended Data Fig. 4, show the gains are equal to within a ~ 10^{-3} fractional error, implying a similarly small ~ 10^{-3} fractional error in the inferred variances and conditional variances, with negligible effect on the squeezing results.

4 Weights—For the first fit to estimate the classical parameters, our data are weighted using an empirical function based on two observations: 1) the polarimeter signal shows increased technical noise in the optical variable at larger imbalance, i.e. when measuring a large instantaneous spin-projection along the z-axis; and 2) points closer in time to t_e should be given greater weight (minimizing errors introduced by small changes in ω_L and T_2 during the measurement). This motivates using the weight function

$$W(\varphi(t_k)) \equiv \frac{g(|t_k - t_e|)}{h(\varphi(t_k))} \quad (45)$$

where $g(|t_k - t_e|) \equiv 1 + A \exp\left(-w\left|\frac{t_k - t_e}{T_2}\right|\right)$ and $h(\varphi_k) = 1 + r|\varphi_k|$. This ensures that we accurately estimated the classical parameters g, ω_L, T_2 and φ_0 at the measurement time t_e.

We numerically optimize $W(\varphi(t_k))$ varying the parameters A, w and r and minimizing the resulting $\mathrm{Tr}(\Gamma_{\mathbf{F}_2|\mathbf{F}_1})$ from the predictive and confirming fits. We find an optimum with the parameters $A = 15$, $w = 11$ and $r = 6$, and note that the fit procedure gives similar results with variations of up to 30% in each of these parameters.

For the predictive and confirming fits, which are linear in F_y and F_z, all the points are weighted equally.

5 Optimal measurement length—The optimal measurement length Δt results from a trade off between the photon shot noise, the decoherences induced by the probing and the technical noise induced by the magnetic field. Longer measurements reduces the photon shot noise, while increasing the atomic decoherences and making the model eq. (2) less accurate. We empirically find the optimal Δt by minimizing the total variance $\mathrm{Tr}(\Gamma_{\mathbf{F}_2|\mathbf{F}_1})$ for measurements with different length, as shown in Extended Data Fig. 5.

6 Conditional Covariance—Estimating $\mathbf{F}$ for several values of t_e gives a predictive trajectory and a confirming one. Estimations are repeated on 453 repetitions of the experiment to gather statistics. Assuming gaussian statistics, to quantify the measurement uncertainty, we compute the conditional covariance matrix

$$\Gamma_{\mathbf{F}_2|\mathbf{F}_1} = \Gamma_{\mathbf{F}_2} - \Gamma_{\mathbf{F}_2\mathbf{F}_1}\Gamma_{\mathbf{F}_1}^{-1}\Gamma_{\mathbf{F}_1\mathbf{F}_2} \quad (46)$$

which quantifies the error in the best linear prediction of $\mathbf{F}_2$ based on $\mathbf{F}_1$.53 Here $\Gamma_{\mathbf{v}}$ indicates the covariance matrix for vector $\mathbf{v}$, and $\Gamma_{\mathbf{uv}}$ indicates the cross-covariance matrix for vectors $\mathbf{u}$ and $\mathbf{v}$. The difference between the best linear prediction of $\mathbf{F}$ using $\mathbf{F}_1$ and the

confirming estimate $\mathbf{F}_2$ is visualized using the vector $\mathscr{F}=\{\mathscr{F}_y,\mathscr{F}_z\}=\tilde{\mathbf{F}}_2-\Gamma_{\mathbf{F}_2\mathbf{F}_1}\Gamma_{\mathbf{F}_1}^{-1}\tilde{\mathbf{F}}_1$, where $\tilde{\mathrm{F}}_i=\mathrm{F}_i-\langle \mathrm{F}_i\rangle$. Standard errors in the estimated conditional covariance matrix are calculated from the statistics of $\{\mathscr{F}\}$.54

Data Availability

The datasets generated and analysed during the current study are available from the corresponding author on reasonable request. The data shown in Fig. 2 and all the data used to generate plots of Extended Data are included as Source Data.

Extended Data

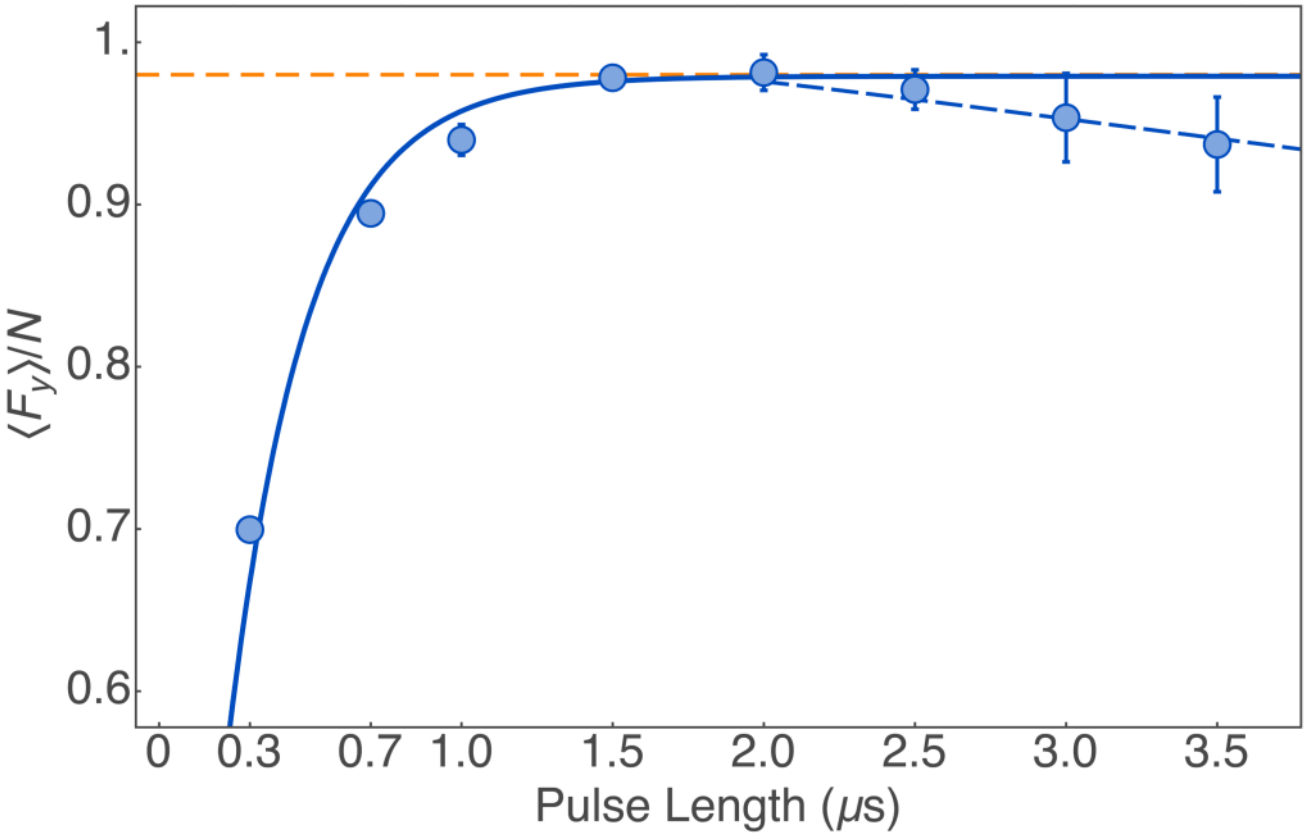

Extended Data Fig. 1.

Optical pumping efficiency. We prepare an input atomic state with $\langle F_y\rangle \simeq N$ via stroboscopic optical pumping in the presence of a small magnetic field along the x-axis. Data is fit with an exponential growing curve $\sim a(1-e^{-t/\tau})$ (solid line) and we obtain $a = 0.979 \pm 0.004$ and $\tau = 0.26 \pm 0.02$. Orange dashed line: Optical pumping efficiency of 98%. ±1 s.e.m. error bars are smaller than the points for most of the data.

Europe PMC Funders Author Manuscripts

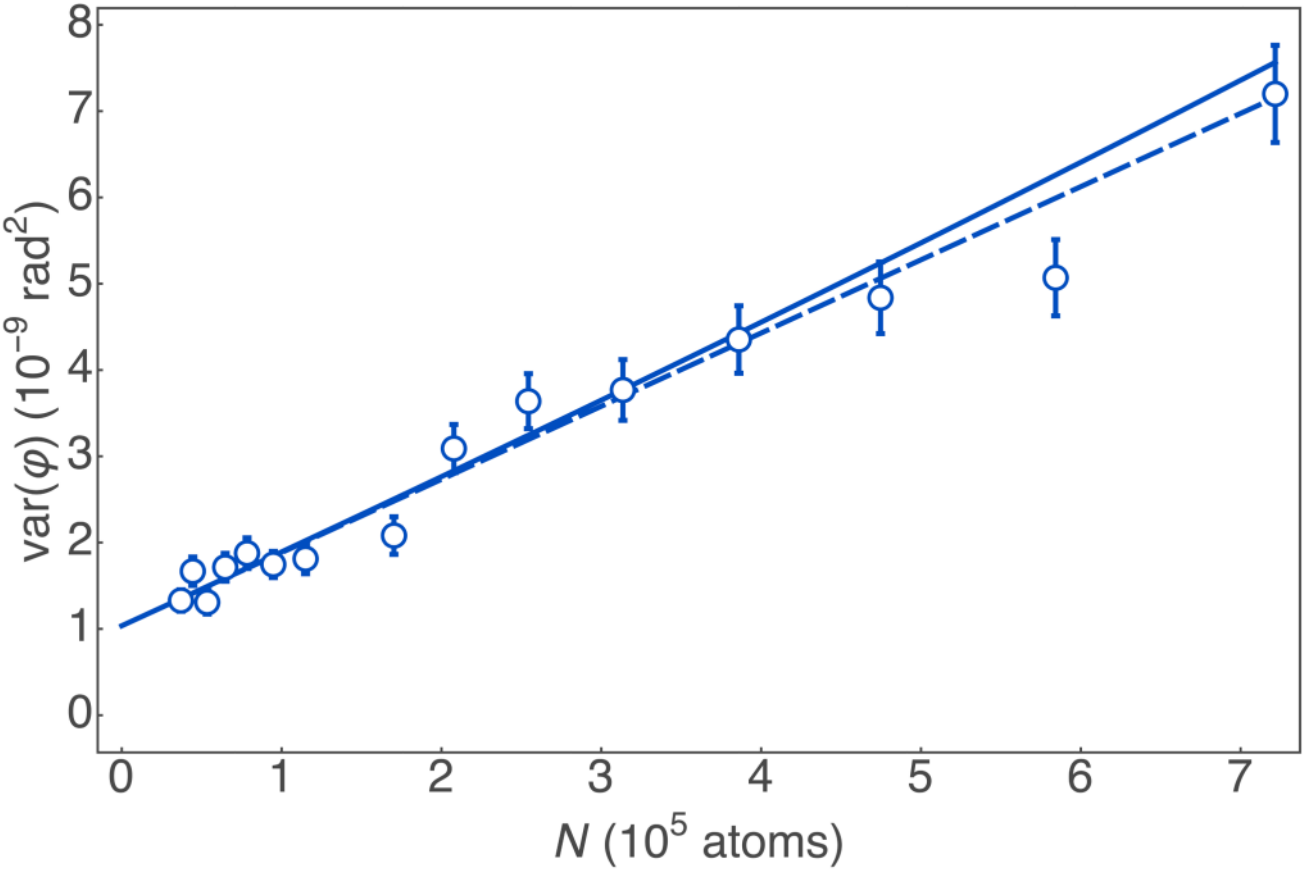

Extended Data Fig. 2.

Calibration of average Faraday rotation signal. We calibrate the rotation angle φ against input atom number N, measured via absorption imaging. Solid line, the fit curve $\varphi = a_0 + \mu_1 N$, with we obtain $\mu_1 = (7.07 \pm 0.04) \times 10^{-8}$ and $a_0 = (3.9 \pm 0.3) \times 10^{-3}$. Error bars indicate ±1 s.e.m.

Europe PMC Funders Author Manuscripts

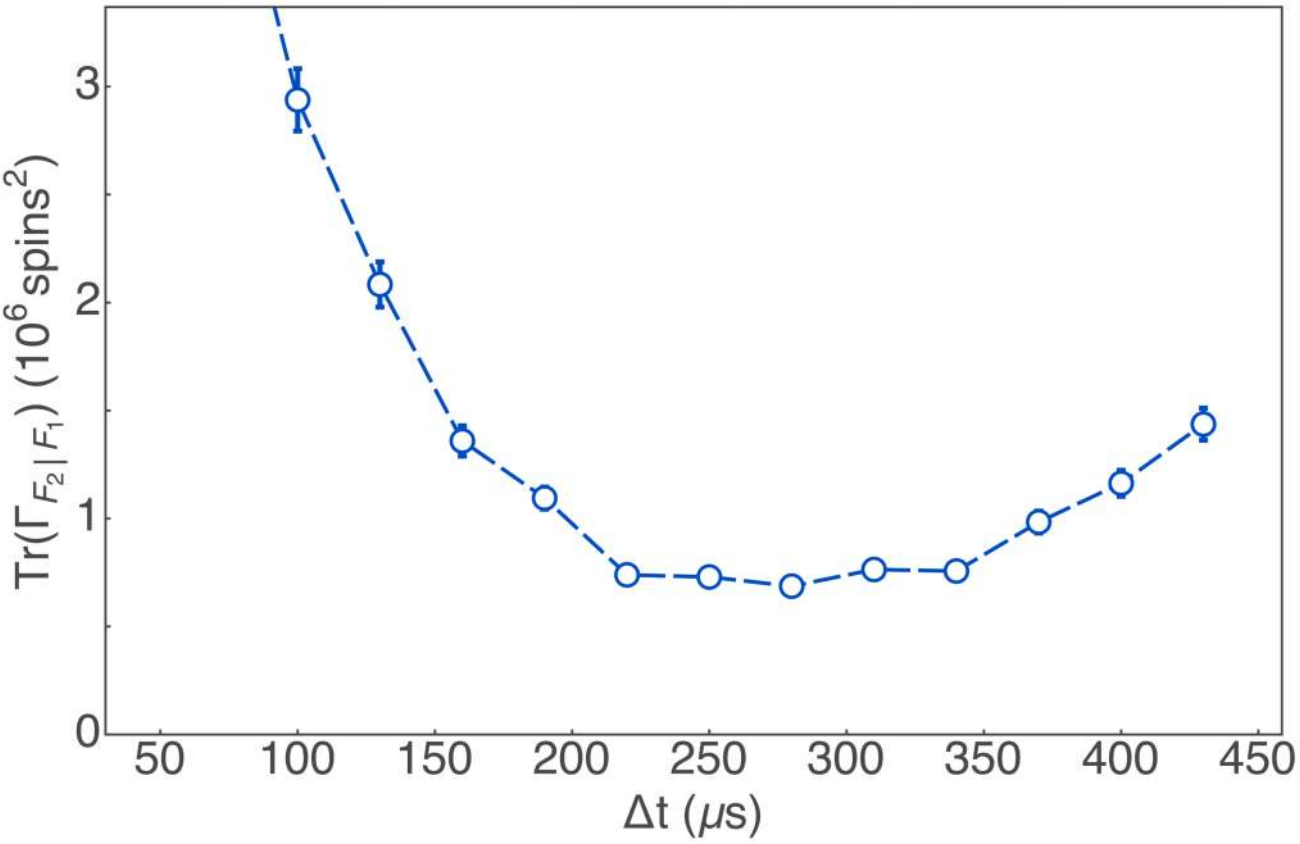

Extended Data Fig. 3.

Calibration of quantum noise limited Faraday rotation probing of atomic spins. We plot the measured variance var(φ) as a function of the number of atoms N in an input coherent spins state with $\langle \mathbf{F} \rangle = \{0, N, 0\}$. Solid curve: a fit using the polynomial var(φ) = $a_0 + a_1 N + a_2 N^2$. The linear term $a_1 = \alpha\mu_2 N/2$ corresponds to the atomic quantum noise from atoms in the input coherent spin state. We estimate $a_0 = (11.7 \pm 0.7) \times 10^{-10}$, $a_1 = (6.5 \pm 0.8) \times 10^{-15}$, and $a_2 = (2.8 \pm 12) \times 10^{-22}$, consistent with negligible technical noise in the atomic state preparation. Dashed line: var(φ) = $a_0 + a_1 N$. Error bars indicate ±1 standard error in the variance for 206 repetitions.

Europe PMC Funders Author Manuscripts

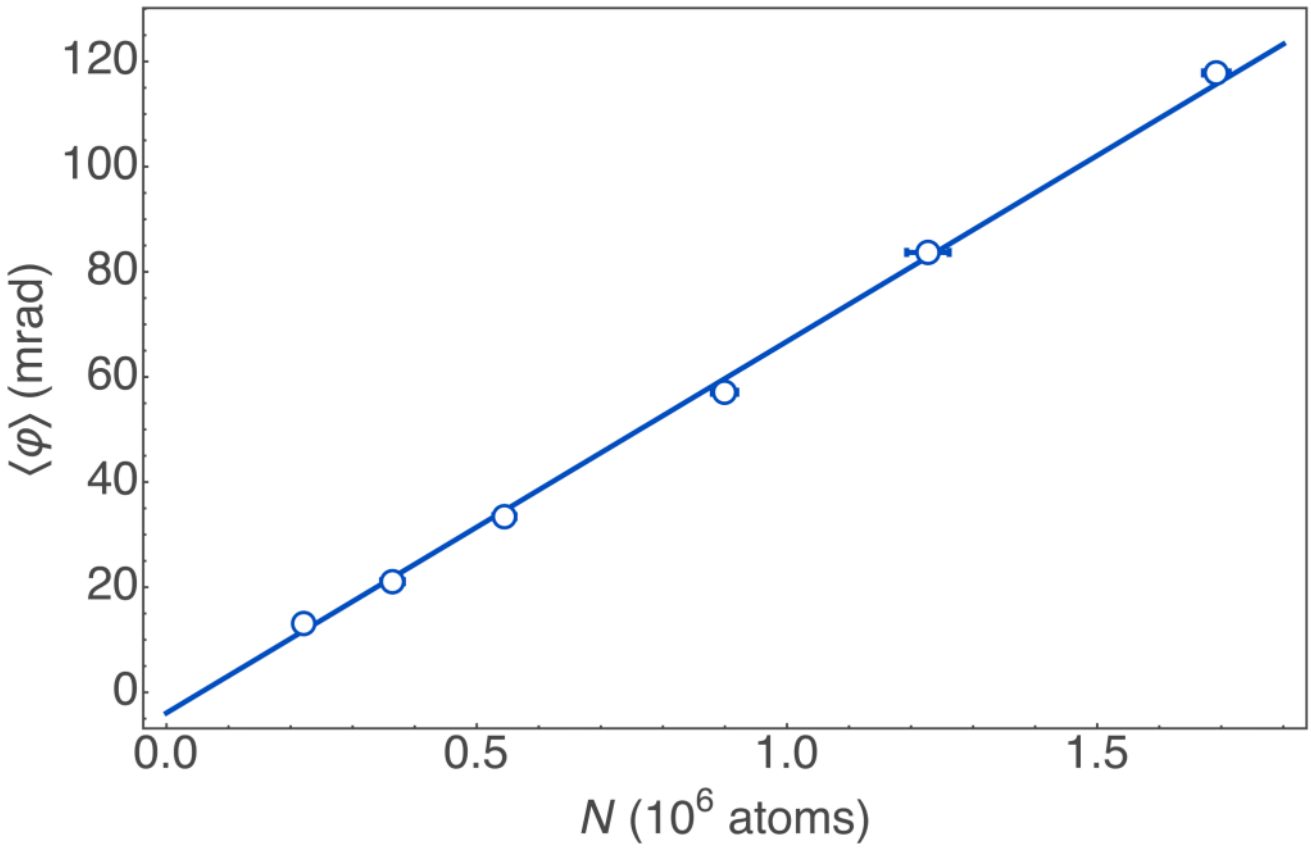

Extended Data Fig. 4.

Fit gain. We compare the estimated F_z and F_y from a fit using Eq. (2); first, with the classical parameters g, ω_L, T_2 and φ_0, fixed (labeled $F_{y,z}^{\{\mathrm{fix}\}}$) for measurements 1 and 2; and second, free to vary as independent parameters (labeled $F_{y,z}^{\{\mathrm{ind}\}}$). In blue (green) F_z (F_y) of the first measurement, in red (orange) F_z (F_y) of the second measurement. A linear fit $\gamma x + \delta$ to points of plots a-d gives $\gamma_a = 0.9981(8)$, $\gamma_b = 1.0026(8)$, $\gamma_c = 0.9923(4)$, $\gamma_d = 1.0007(5)$ and $\delta_a = 0.003(1)$, $\delta_b = 0.0001(9)$, $\delta_c = 0.0004(3)$, $\delta_d = -0.0023(3)$, where the subscripts refer to the values shown in plots a-d. A grey line $y = x$ is plotted on both the figures.

Europe PMC Funders Author Manuscripts

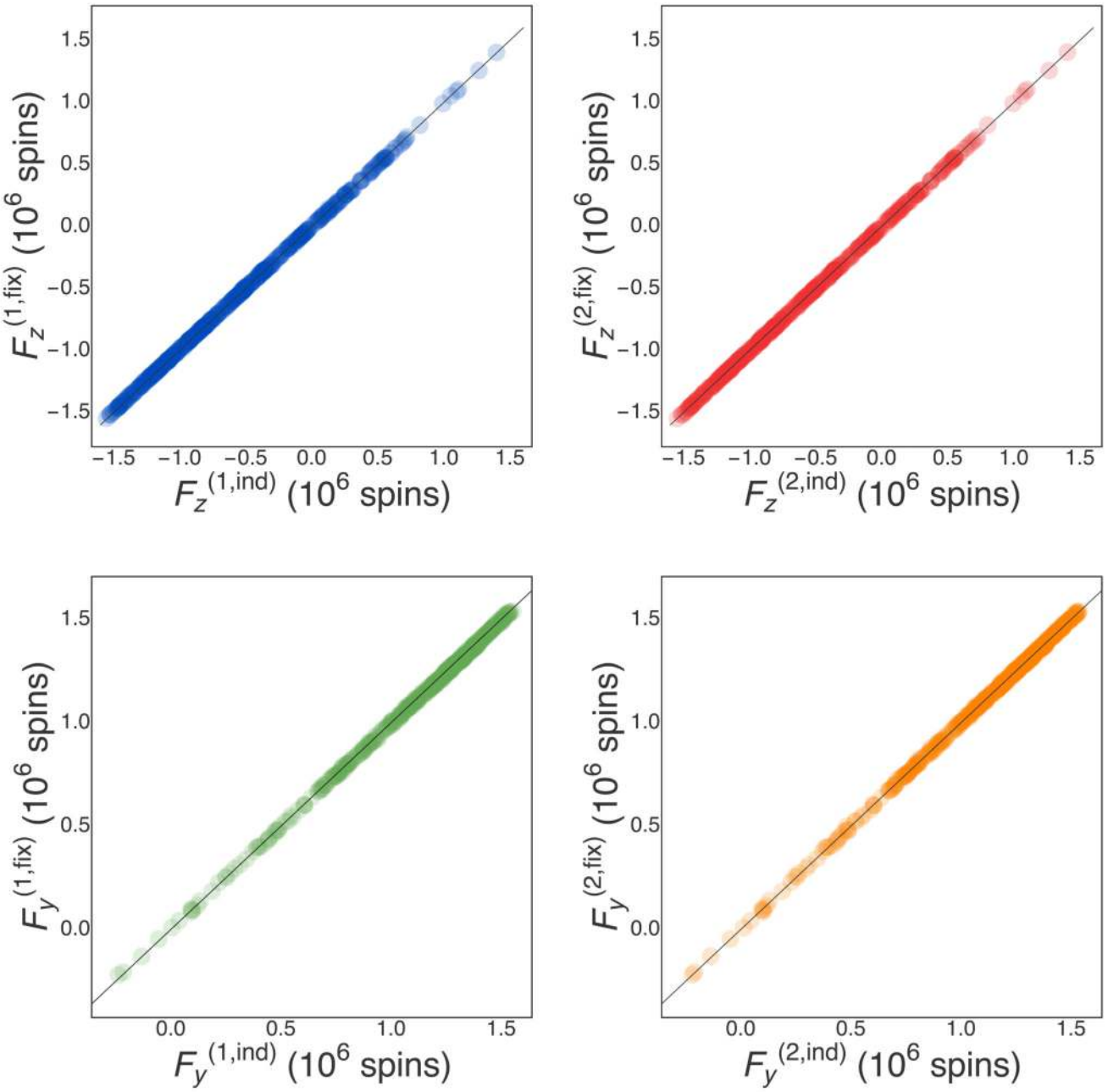

Extended Data Fig. 5.

Tracking precision as function of Δt. An optimum is found at $\Delta t = 270$ μs. Error bars indicate ±1 standard error in the variance for 453 repetitions.

Acknowledgements

We thank L. Bianchet, G. Vitagliano, M. D. Reid, P. D. Drummond, G. Tóth, N. Behbood, M. Napolitano, S. Palacios, D. T. Campbell and M. M. Fria. Work supported by MINECO/FEDER, MINECO projects MAQRO (Ref. FIS2015-68039-P), XPLICA (FIS2014-62181-EXP) and Severo Ochoa grant SEV-2015-0522, Catalan 2014-SGR-1295, by the European Union Project QUIC (grant agreement 641122), European Research Council project AQUMET (grant agreement 280169) and ERIDIAN (grant agreement 713682), and by Fundació Privada CELLEX.

References

1. Kominis I, Kornack T, Allred J, Romalis M. A subfemtotesla multichannel atomic magnetometer. Nature. 2003; 422:596. [PubMed: 12686995]
2. Ludlow AD, Boyd MM, Ye J, Peik E, Schmidt PO. Optical atomic clocks. Rev Mod Phys. 2015; 87:637.
3. Dang HB, Maloof AC, Romalis MV. Ultrahigh sensitivity magnetic field and magnetization measurements with an atomic magnetometer. Appl Phys Lett. 2010; 97 151110.
4. Gomes MD, Dao P, Jeong K, Slack CC, Vassiliou CC, Finbloom JA, Francis MB, Wemmer DE, Pines A. ^{129}Xe NMR relaxation-based macromolecular sensing. J Am Chem Soc. 2016; 138:9747. [PubMed: 27472048]
5. Wolf T, Neumann P, Nakamura K, Sumiya H, Ohshima T, Isoya J, Wrachtrup J. Subpicotesla diamond magnetometry. Phys Rev X. 2015; 5 041001.
6. Jensen K, Budvytyte R, Thomas RA, Wang T, Fuchs AM, Balabas MV, Vasilakis G, Mosgaard LD, Stærkind HC, Müller JH, Heimburg T, et al. Non-invasive detection of animal nerve impulses with an atomic magnetometer operating near quantum limited sensitivity. Sci Rep. 2016; 6 29638.
7. Plewes DB, Kucharczyk W. Physics of MRI: A primer. J Magn Reson Imaging. 2012; 35:1038. [PubMed: 22499279]
8. He QY, Peng S-G, Drummond PD, Reid MD. Planar quantum squeezing and atom interferometry. Phys Rev A. 2011; 84 022107.
9. Robertson HP. The uncertainty principle. Phys Rev. 1929; 34:163.
10. Dammeier L, Schwonnek R, Werner RF. Uncertainty relations for angular momentum. New J Phys. 2015; 17 093046.
11. Grangier P, Levenson JA, Poizat J-P. Quantum non-demolition measurements in optics. Nature. 1998; 396:537.
12. Koschorreck M, Napolitano M, Dubost B, Mitchell MW. Quantum nondemolition measurement of large-spin ensembles by dynamical decoupling. Phys Rev Lett. 2010; 105 093602.
13. Sewell RJ, Napolitano M, Behbood N, Colangelo G, Mitchell MW. Certified quantum non-demolition measurement of a macroscopic material system. Nat Photon. 2013; 7:517.
14. Béguin J-B, Bookjans EM, Christensen SL, Sørensen HL, Müller JH, Polzik ES, Appel J. Generation and detection of a sub-poissonian atom number distribution in a one-dimensional optical lattice. Phys Rev Lett. 2014; 113 263603.
15. Lodewyck J, Westergaard PG, Lemonde P. Nondestructive measurement of the transition probability in a Sr optical lattice clock. Phys Rev A. 2009; 79 061401.
16. Sander TH, Preusser J, Mhaskar R, Kitching J, Trahms L, Knappe S. Magnetoencephalography with a chip-scale atomic magnetometer. Biomed Opt Express. 2012; 3:981. [PubMed: 22567591]
17. Sheng D, Li S, Dural N, Romalis MV. Subfemtotesla scalar atomic magnetometry using multipass cells. Phys Rev Lett. 2013; 110 160802.
18. Hosten O, Engelsen NJ, Krishnakumar R, Kasevich MA. Measurement noise 100 times lower than the quantum-projection limit using entangled atoms. Nature. 2016; 529:505. [PubMed: 26751056]
19. Hall LT, Cole JH, Hill CD, Hollenberg LCL. Sensing of fluctuating nanoscale magnetic fields using nitrogen-vacancy centers in diamond. Phys Rev Lett. 2009; 103 220802.
20. Bienfait A, Pla JJ, Kubo Y, Stern M, Zhou X, Lo CC, Weis CD, Schenkel T, Thewalt MLW, Vion D, Esteve D, et al. Reaching the quantum limit of sensitivity in electron spin resonance. Nat Nanotechnol. 2016; 11:253. [PubMed: 26657787]
21. Budker D, Romalis M. Optical magnetometry. Nature Phys. 2007; 3:227.
22. Miffre A, Jacquey M, Buchner M, Trenec G, Vigue J. Atom interferometry. Phys Scr. 2006; 74:C15.
23. Yurke B, McCall SL, Klauder JR. Su(2) and su(1,1) interferometers. Phys Rev A. 1986; 33 4033.
24. Colangelo G, Sewell RJ, Behbood N, Ciurana FM, Triginer G, Mitchell MW. Quantum atom–light interfaces in the gaussian description for spin-1 systems. New J Phys. 2013; 15 103007.
25. Braginsky VB, Vorontsov YI, Thorne KS. Quantum nondemolition measurements. Science. 1980; 209:547. [PubMed: 17756820]

26. Tsang M, Caves CM. Evading quantum mechanics: Engineering a classical subsystem within a quantum environment. Phys Rev X. 2012; 2 031016.
27. Polzik ES, Hammerer K. Trajectories without quantum uncertainties. Ann Phys. 2015; 527:A15.
28. Smith GA, Chaudhury S, Silberfarb A, Deutsch IH, Jessen PS. Continuous weak measurement and nonlinear dynamics in a cold spin ensemble. Phys Rev Lett. 2004; 93 163602.
29. Koschorreck M, Napolitano M, Dubost B, Mitchell MW. Sub-projection-noise sensitivity in broadband atomic magnetometry. Phys Rev Lett. 2010; 104 093602.
30. Ciurana FM, Colangelo G, Sewell RJ, Mitchell MW. Real-time shot-noise-limited differential photodetection for atomic quantum control. Opt Lett. 2016; 41:2946. [PubMed: 27367072]
31. Kubasik M, Koschorreck M, Napolitano M, de Echaniz SR, Crepaz H, Eschner J, Polzik ES, Mitchell MW. Polarization-based light-atom quantum interface with an all-optical trap. Phys Rev A. 2009; 79 043815.
32. Deutsch IH, Jessen PS. Quantum control and measurement of atomic spins in polarization spectroscopy. Optics Communications. 2010; 283:681.
33. Kuzmich A, Mandel L, Bigelow NP. Generation of spin squeezing via continuous quantum nondemolition measurement. Phys Rev Lett. 2000; 85:1594. [PubMed: 10970566]
34. Appel J, Windpassinger PJ, Oblak D, Hoff UB, Kjær-gaard N, Polzik ES. Mesoscopic atomic entanglement for precision measurements beyond the standard quantum limit. Proc Nat Acad Sci. 2009; 106 10960.
35. Ciurana FM, Colangelo G, Sewell RJ, Mitchell MW. Real-time shot-noise-limited differential photodetection for atomic quantum control. Opt Lett. 2016; 41:2946. [PubMed: 27367072]
36. Gühne O, Tóth G. Entanglement detection. Phys Rep. 2009; 474:1.
37. Sørensen AS, Mølmer K. Entanglement and extreme spin squeezing. Phys Rev Lett. 2001; 86 4431.
38. Béguin J-B, Bookjans EM, Christensen SL, Sørensen HL, Müller JH, Polzik ES, Appel J. Generation and detection of a sub-poissonian atom number distribution in a one-dimensional optical lattice. Phys Rev Lett. 2014; 113 263603.
39. Schlosser N, Reymond G, Protsenko I, Grangier P. Sub-poissonian loading of single atoms in a microscopic dipole trap. Nature. 2001; 411:1024. [PubMed: 11429597]
40. Hofmann CS, Günter G, Schempp H, Robert-de Saint-Vincent M, Gärttner M, Evers J, Whitlock S, Weidemüller M. Sub-Poissonian statistics of Rydberg-interacting dark-state polaritons. Phys Rev Lett. 2013; 110 203601.
41. Gajdacz M, Hilliard AJ, Kristensen MA, Pedersen PL, Klempt C, Arlt JJ, Sherson JF. Preparation of ultracold atom clouds at the shot noise level. Phys Rev Lett. 2016; 117 073604.
42. Hosten O, Engelsen NJ, Krishnakumar R, Kasevich MA. Measurement noise 100 times lower than the quantum-projection limit using entangled atoms. Nature. 2016; 529:505. [PubMed: 26751056]
43. Stockton, JK. Continuous quantum measurement of cold alkali-atom spins. Ph.D. thesis, California Institute of Technology; 2007.
44. Takano T, Fuyama M, Namiki R, Takahashi Y. Spin squeezing of a cold atomic ensemble with the nuclear spin of one-half. Phys Rev Lett. 2009; 102 033601.
45. Schleier-Smith MH, Leroux ID, Vuletić V. States of an ensemble of two-level atoms with reduced quantum uncertainty. Phys Rev Lett. 2010; 104 073604.
46. Sewell RJ, Koschorreck M, Napolitano M, Dubost B, Behbood N, Mitchell MW. Magnetic sensitivity beyond the projection noise limit by spin squeezing. Phys Rev Lett. 2012; 109 253605.
47. Bohnet JG, Cox KC, Norcia MA, Weiner JM, Chen Z, Thompson JK. Reduced spin measurement back-action for a phase sensitivity ten times beyond the standard quantum limit. Nat Photon. 2014; 8:731.
48. Colangelo G, Sewell RJ, Behbood N, Ciurana FM, Triginer G, Mitchell MW. Quantum atom–light interfaces in the gaussian description for spin-1 systems. New J Phys. 2013; 15 103007.
49. Madsen LB, Mølmer K. Spin squeezing and precision probing with light and samples of atoms in the gaussian description. Phys Rev A. 2004; 70 052324.
50. Koschorreck M, Napolitano M, Dubost B, Mitchell MW. Sub-projection-noise sensitivity in broadband atomic magnetometry. Phys Rev Lett. 2010; 104 093602.

51. Koschorreck M, Napolitano M, Dubost B, Mitchell MW. Quantum nondemolition measurement of large-spin ensembles by dynamical decoupling. Phys Rev Lett. 2010; 105 093602.

52. Sewell RJ, Napolitano M, Behbood N, Colangelo G, Mitchell MW. Certified quantum non-demolition measurement of a macroscopic material system. Nat Photon. 2013; 7:517.

53. Behbood N, Martin Ciurana F, Colangelo G, Napolitano M, Tóth G, Sewell RJ, Mitchell MW. Generation of macroscopic singlet states in a cold atomic ensemble. Phys Rev Lett. 2014; 113 093601.

54. Kendall, M., Stuart, A. The advanced theory of statistics. Vol. 2. London: Griffin; 1979.

Europe PMC Funders Author Manuscripts

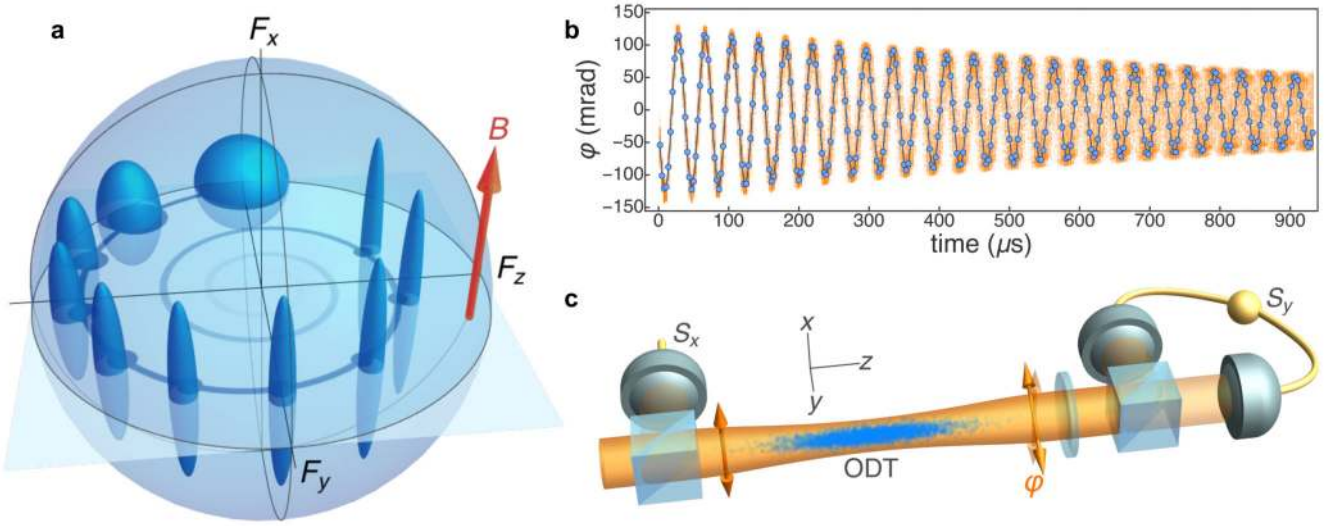

Fig. 1. Simultaneous, precise tracking of spin angle and amplitude.

a) Bloch-sphere representation of the atomic state evolution. Ellipsoids show uncertainty volumes (not to scale) as the state evolves anti-clockwise from an initial, F_y-polarized state with isotropic uncertainty. An *x*-oriented magnetic field **B** drives a coherent spin precession in the F_y–F_z plane. Quasi-continuous measurement of F_z produces a reduction in F_z and F_y variances, with a corresponding increase in var(F_x). b) Observed Faraday rotation angle $\varphi \propto F_z$ versus time. Each circle shows the rotation angle from one V-polarized pulse. A magnetic field of 37.6 mG produces the observed oscillation, while dephasing due to residual magnetic gradients and off-resonant scattering of probe photons cause the decay of coherence. Blue circles show a single, representative trace, overlaid on 453 repetitions of the experiment shown as orange dots. The time zero corresponds to the first probe pulse; the end of optical pumping is 58 μs earlier. c) Experimental geometry: 1.9×10^6 cold ^{87}Rb atoms are confined in a weakly-focused single beam optical dipole trap (ODT). Transverse optical pumping is used to produce F_y polarisation. On-axis, 0.6 μs pulses with mean photon number 2.74×10^6 experience Faraday rotation by an angle $\varphi \propto F_z$. A polarimeter consisting of waveplates, a polarising beamsplitter, high-quantum-efficiency photodiodes, and charge-sensitive amplifiers measures the output Stokes component S_y. A reference detector before the atoms measures input Stokes component $S_0 = |S_x|$. The rotation angle is computed as $\varphi = \arcsin(S_y/S_x)$.

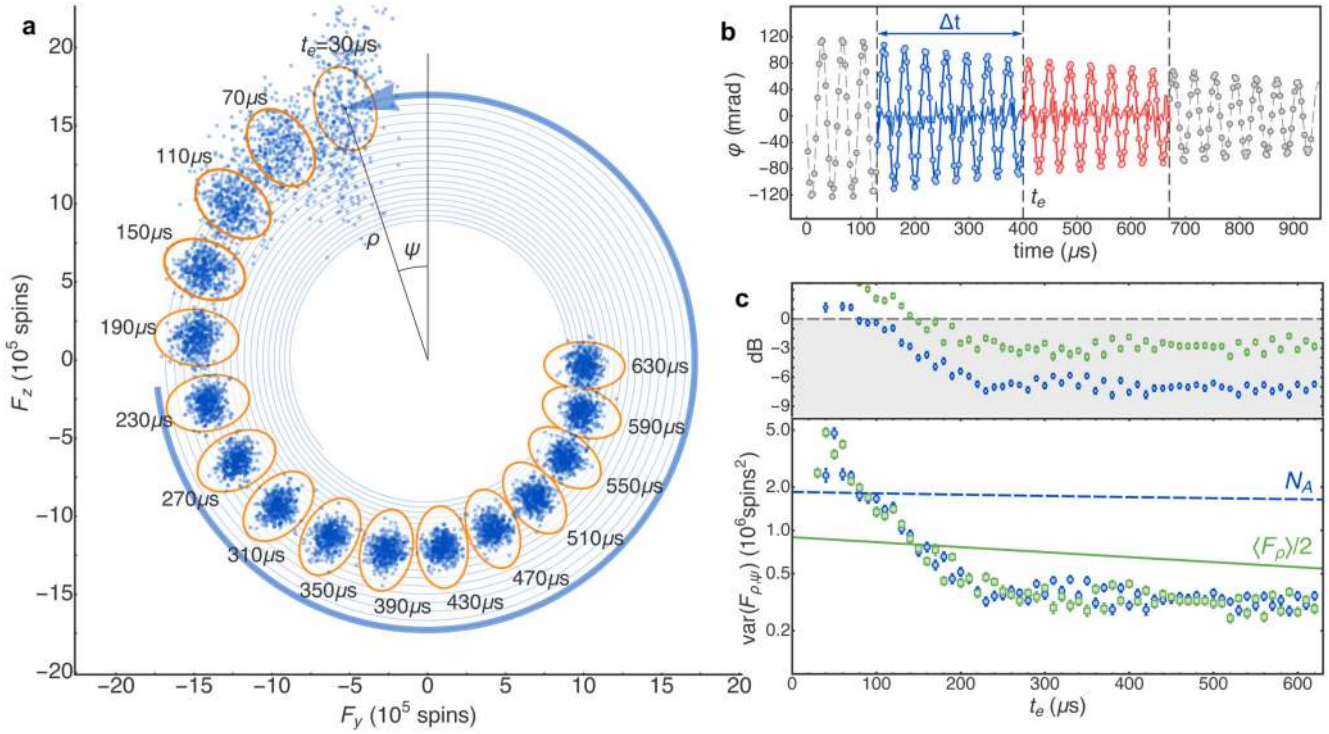

Fig. 2. Experimental results.

a) Measured trajectories in the F_y–F_z phase space at different estimation times t_e. For each of the 453 traces shown in Fig. 1 b), the function of Eq. (2) is fit to the data to find predictive and confirming estimates $\mathbf{F}_1$, $\mathbf{F}_2$, respectively, for (F_y, F_z) at time t_e. Fits for $\mathbf{F}_1$ and $\mathbf{F}_2$ use disjoint sets of data covering the ranges $t_e - \Delta t \leq t_k < t_e$ and $t_e < t_k \leq t_e + \Delta t$, respectively. A single fit is a tightly-wound spiral shown as a thin blue line and the thick arrow shows the trajectory from $t = 0$ to $t = t_e = 30$ μs. For clarity, we show results for t_e values spaced by 40 μs, slightly more than one Larmor period. Each point shows $\langle \mathbf{F}_1 \rangle + 100\mathscr{F}$, where $\langle \mathbf{F}_1 \rangle$ is the mean over the 453 repetitions, and $\mathscr{F} \equiv \mathbf{F}_2 - \Gamma_{2,1}\Gamma_1^{-1}\mathbf{F}_1$ is the error of the best linear prediction (see SI). The factor 100 provides magnification for visualization purposes. Orange ellipses, with radial and azimuthal radii of 2σ, where $\sigma = 100\sqrt{\mathrm{CL}}$, show the relevant classical limits: Poisson (radial, CL = N) and SQL (azimuthal, CL = $\langle F_\rho \rangle/2$). b) Fits to estimate (F_y, F_z) for $t_e = 400$ μs and a measurement time $\Delta t = 270$ μs. Blue (red) shows fits based on prior (posterior) data. Shaded regions show fit residuals ×10. c) Evolution of tracking precision for different t_e. Blue circles and green squares show radial and azimuthal components of $\Gamma_{\mathbf{F}_2|\mathbf{F}_1}$. Error bars show the ±1 standard error in the variance for 453 repetitions. Dashed blue and solid green curves show Poisson and SQL variances. These decrease during probing due to loss of coherence and loss of atoms. No readout noise has been subtracted.

Europe PMC Funders Author Manuscripts